Structured ultrasound-modulated optical tomography

Maïmouna Bocoum, Jean-Luc Gennisson, Jean-Baptiste Laudereau, Anne Louchet-Chauvet, Jean-Michel Tualle, François Ramaz

Research Article Vol. 58, No. 8 / 10 March 2019 / Applied Optics 1933

applied optics

Structured ultrasound-modulated optical tomography

Maïmouna Bocoum,[1,*] Jean-Luc Gennisson,[2] Jean-Baptiste Laudereau,[1] Anne Louchet-Chauvet,[3] Jean-Michel Tualle,[4] and François Ramaz[1]

[1]Institut Langevin, Ondes et Images—ESPCI Paris, PSL Research University, CNRS UMR 7587, INSERM U979, Université Paris VI Pierre et Marie Curie, 1 rue Jussieu, 75005 Paris, France
[2]Imagerie par Résonance Magnétique Médicale et Multi-Modalités CNRS UMR8081, Université Paris Sud, CEA Service Hospitalier Frédéric Joliot 4, Place du Gal Leclerc 91401 Orsay Cedex, France
[3]Laboratoire Aimé Cotton, CNRS UMR9188, Univ Paris-Sud, ENS Cachan, Université Paris-Saclay, batiment 505, campus d'Orsay, 91400 ORSAY, France
[4]Laboratoire de Physique des Lasers, CNRS UMR7538, Université Paris Nord 13, 99 Ave J.B. Clément, F-93430 Villetaneuse, France
*Corresponding author: maimouna.bocoum@espci.fr

Received 19 September 2018; revised 11 January 2019; accepted 31 January 2019; posted 1 February 2019 (Doc. ID 346368); published 6 March 2019

Ultrasound-modulated optical tomography (UOT) is an imaging technique that couples light and ultrasound in order to perform in-depth imaging of highly scattering media. In previous work, we introduced plane wave UOT, an imaging method analogous to x-ray tomography based on the filtered backprojection for image reconstruction. Angle-limited measurements, however, led to drastic loss of lateral spatial resolution. Here, we present a new structured ultrasonic plane wave UOT method that allows partial recovery of the resolution. For image reconstruction, we present a generalization of the Fourier slice theorem along with a generalized filtered backprojection formalism. The method is successfully tested on simulated and experimental data.

https://doi.org/10.1364/AO.58.001933

1. INTRODUCTION

Ultrasound-modulated optical tomography [1–3] (UOT) is an imaging technique which couples light and ultrasound (US) to perform in-depth optical imaging of highly scattering media. For depths typically greater than 1 mm, multiple light scattering of biological tissues makes conventional optical imaging techniques inadequate. In UOT, an optically diffuse medium is illuminated with a single longitudinal mode laser at frequency f_L. The propagation of ballistic US inside the medium induces a modulation of the light temporal phase through the acousto-optic (AO) effect [4]. Photons having undergone this phase modulation are said to have been "tagged." A few-cycle US pulse focused into the medium propagates in a straight line across its Rayleigh range at a velocity $c_s \sim 1500$ m/s. If the detection of modulated light is fast enough to track US propagation, the detection of tagged photons provides a direct mapping of the local absorption and/or diffusion contrast along the line with US spatial resolution [5]. Fast detection techniques include extended Fabry–Perot cavities [5], spectral hole burning [6], or, as used in the present work, self-adaptive wavefront holography [7,8].

By using an US transducer array, two-dimensional UOT images are constructed line by line by sweeping electronically the US propagation axis along the transducer array. For each position, the AO signal is recorded and stacked to build the UOT image [9,10]. We refer to this as "focused waves" (FW) UOT. In previous work, we introduced an alternative approach using "plane waves" (PWs) [11], thereby reducing the overall acquisition time by an order of magnitude. In PW-UOT, one acquisition is performed by sending a few-cycle plane US wave at a fixed angle, and reproducing this for a large angular span from which the original image can be reconstructed. This approach is identical to x-ray computed tomography (CT), positron emission tomography, or electron tomography, which all rely on the Radon inversion principle [12–14]. The PW emission angle is, however, limited to $\pm 20°$ because of the finite directivity of US probes, leading to a substantial loss in lateral resolution. This lack of resolution stems from the ill-posed nature of the problem consisting in reconstructing an object from a limited number of its projections. This so-called limited-angle tomography problem is encountered in various fields of physics, such as non-destructive testing [15] limited by geometrical congestion, or in CT scans where exposure time is reduced for safety reasons [16]. The corresponding inversion problem has been massively described and investigated [17–20], and the image reconstruction fidelity

varies from one procedure to the other. In most practical cases, however, the filtered-backprojection method is preferred because of its simplicity of implementation and low computational cost.

The particularity of PW-UOT over standard tomography resides in our ability to control the shape of the acoustic envelope sent into the medium. In this paper, we show that the final resolution of an imaged object after reconstruction is increased when adding structure to the US wavefront. The idea of using structured waves (SWs) to improve spatial resolution is not new and was applied, for example, in super-resolved confocal microscopy [21–23]. In other work related to UOT, temporal structure was used on the acoustic field to recover a spatial resolution in the direction of US propagation [24–26]. Here, we present a generalization of the angle-limited tomography problem when spatial structure is transversely added to the acoustic wave. This leads to a generalized form of the Fourier slice theorem (FST) as well as an analytic backprojection inversion. We finally show experimentally the ability of the method to partially recover the lateral resolution of an image.

2. PRINCIPLE OF THE METHOD

In PW-UOT, all piezo-elements of the probe emit a few-cycle US pulse with a linear phase delay resulting in the propagation of a uniform acoustic wavefront at angle θ. In the plane defined by the position of the US probe, we define $I(x,z)$ as the distribution of signal density, which accounts for laser illumination, the qualitative absorption properties of the medium, as well as collection and detection of tagged photons. PW-UOT aims at reconstructing $I(x,z)$ from a finite number of its angular projections. The principle is illustrated in Fig. 1(a) for an arbitrary $\theta > 0$.

To first order approximation, the flux of tagged photons is known to be quadratic with the US temporal envelope [27], which gives a theoretical expression in Eq. (1) for the recorded signal $s(c_s t,\theta)$, where t is the time following the US burst emission, $\tilde{P}(c_s t,x,z)$ is the pressure field envelope normalized

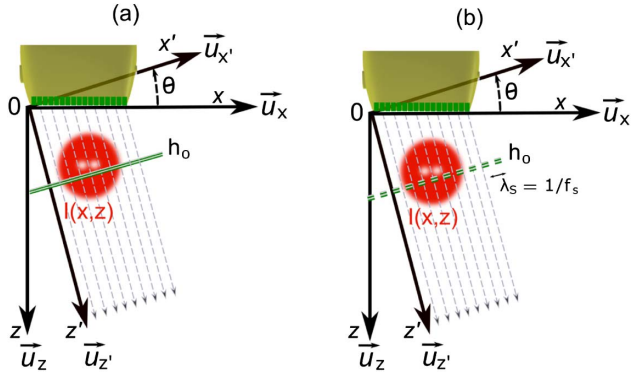

Fig. 1. PW-UOT where a short acoustic burst propagates along direction z' at velocity $c_s \sim 1500$ m/s. (a) PW-UOT used in [11] with pulse envelope $h_0(x') = 1$, meaning all piezo-elements are active. (b) SW-UOT where h_0 is a periodic spatial step function of frequency f_s created by turning either on or off the piezo-elements along the transducer array.

to its maximum value in order to be dimensionless, and $c_s \sim 1500$ m/s is the sound velocity. We consider the US pulse with spatial envelope h_0 as infinitely short in time such that the acoustic temporal profile is represented by a Dirac function. Within the scope of this paper, $h_0(x)$ takes discrete values equal to either 0 or 1, such that $h_0^2(x) = h_0(x)$, which leads to a simple expression Eq. (2) for the recorded signal:

$$s(c_s t,\theta) = \int_{x,z} I(x,z)\tilde{P}^2(c_s t,x,z)\mathrm{d}x\mathrm{d}z \tag{1}$$

$$\approx \int_{x,z} I(x,z)h_0\Big(\underbrace{x\cos\theta - z\sin\theta}_{x'}\Big)\delta\Big(\underbrace{z\cos\theta + x\sin\theta}_{z'} - c_s t\Big)\mathrm{d}x\mathrm{d}z, \tag{2}$$

where $x' = x\cos\theta - z\sin\theta$ and $z' = z\cos\theta + x\sin\theta$ are the Cartesian coordinates after a rotation of angle θ. In the case of plane waves, we have $h_0 = 1$. Therefore, by writing $\tilde{s}(f_t,\theta)$, the Fourier transform of $s(c_s t,\theta)$ along parameter $c_s t$, we get

$$\tilde{s}(f_t,\theta) = \int_{x,z} I(x,z)e^{-2i\pi f_t(x\sin\theta + z\cos\theta)}\mathrm{d}x\mathrm{d}z \tag{3}$$

$$= \mathcal{F}_{x,z}(I)(f_t\sin\theta, f_t\cos\theta), \tag{4}$$

where $\mathcal{F}_u(.)$ refers to the Fourier transform along parameter u. In the following, f_t designates the spatial frequency dual to variable $c_s t$ and (f_x, f_z) the dual frequencies of variable (x,z). Equation (4) leads to the FST formally known as

$$\mathcal{F}_{c_s t}(s(c_s t,\theta)) = \mathcal{F}_{x,z}(I)(f_t\sin\theta, f_t\cos\theta), \tag{5}$$

which provides a relation between each measurement at a given θ angle with a line along one polar direction of the Fourier plane of object $I(x,z)$. Inverting Eq. (5) when the problem is well-posed, i.e., for $\theta \in [0, 2\pi]$, is easily done using polar coordinates in the Fourier domain [17], and yields

$$I(x,z) = \int_0^{2\pi}\int_{f_t=0}^{\infty} \tilde{s}(f_t,\theta)e^{2i\pi z' f_t} f_t \mathrm{d}f_t\mathrm{d}\theta. \tag{6}$$

Experimentally, θ is limited in all scans by θ_m, the maximum angle allowed by the US probe directivity. As well-described in the literature [17], Eq. (6) is the starting point in the derivation of the filtered backprojection (FBP), the final expression of which is given using following Eq. (7):

$$I_{\mathrm{rec}}(x,z) = \int_{-\theta_m}^{\theta_m}\int_{f_t=-\infty}^{\infty} |f_t| S_{f_c}(f_t)\tilde{s}(f_t,\theta)e^{i2\pi z' f_t}\mathrm{d}f_t\mathrm{d}\theta, \tag{7}$$

where $S_{f_c}(.)$ is a low-pass *Ram-Lak* filter [28] required to reduce non-physical influence of frequencies above the cutoff frequency f_c, and $I_{\mathrm{rec}}(x,z)$ designates the reconstructed image. In all reconstructions presented in this paper, we use the FBP with an angular window centered around 0°, with $\theta_m = 20°$. As already explained in [11], $I_{\mathrm{rec}}(x,z)$ suffers from a strong degradation of its lateral resolution because all spectral components outside the $\pm\theta_m$ finite cone in the Fourier domain are lost (cf. blue cone represented in Fig. 2).

A. Generalization of the FST Using Structured Acoustic Waves

For each angle θ, the acquisition is done by spatially structuring the acoustic field emitted by the US probe, as depicted in Fig. 1(b). In this respect, piezo-elements are turned either on or off such that the acoustic envelope profile is a periodic step function of frequency $f_s = 1/\lambda_s$, where λ_s is the structuring period. In order to access complex information in the Fourier plane of object $I(x,z)$, an acquisition is repeated four times in quadrature for a given structure. This approach is similar to multiple-phase spatial or spectral holography [29–31]. We call ϕ the absolute phase of the structured wavefront associated with the spatial modulation of frequency f_s. The Fourier decomposition of function $h_0(x')$ is the sum of a positive constant equal to its average over one period λ_s and harmonic terms of frequency f_c. For the sake of clarity, we use an approximated expression for the envelope limited to its first harmonic such that $h_0(x') \approx \frac{1}{2} + \frac{2}{\pi}\cos(2\pi f_s x' + \phi))$. This approximation is justified because the first harmonic contains ~80% of the overall harmonic energy. The corresponding UOT measurement, according to Eq. (2), is given by

$$s_\phi(c_s t, \theta, f_s) = \int_{x,z} I(x,z)\left(\frac{1}{2} + \frac{2}{\pi}\cos(2\pi f_s x' + \phi)\right) \times \delta(z' - c_s t)\mathrm{d}x\mathrm{d}z. \quad (8)$$

By performing four distinct measurements with $\phi = 0; \frac{\pi}{2}; \pi$ and $\frac{3\pi}{2}$, we retrieve the Fourier component of the object along direction x' using the linear combination:

$$s(c_s t, \theta, f_s) = \frac{(s_0 - s_\pi) - i(s_{\frac{\pi}{2}} - s_{\frac{3\pi}{2}})}{2/\pi} = \int_{x,z} I(x,z) e^{-2i\pi f_s x'} \delta(z' - c_s t)\mathrm{d}x\mathrm{d}z, \quad (9)$$

where $i^2 = -1$. Taking the Fourier transform of Eq. (9) with respect to variable $c_s t$, we find the following generalized FST relation:

$$\mathcal{F}_{c_s t}(s(c_s t, \theta, f_s)) = \mathcal{F}_{x,z}(I)(f_t \sin\theta + f_s \cos\theta, f_t \cos\theta - f_s \sin\theta). \quad (10)$$

In Fig. 2, we represent the accessible Fourier plane region in SW-UOT when $-20° \le \theta \le 20°$, derived from Eq. (10). The PW-UOT cone (i.e., the non-structured case where $f_s = 0$) is represented in blue. For the same angular span and with an arbitrary value $f_s = 1$ mm^{-1}, the SW-UOT domain is represented in orange and corresponds to the vertical line tangent to a circle of radius f_s. Because we explore the Fourier transform of a real object, components corresponding to θ and $\theta + \pi$ are directly known through conjugated symmetry. This shows how structuring the acoustic envelope allows the exploration of the lateral region of the Fourier domain, thereby recovering spatial information in the direction orthogonal to propagation. The question that naturally arises is how to reconstruct the object from its partial projections in the Fourier domain when performing an arbitrary SW-UOT measurement.

We introduce two methods to reconstruct the object. The first method, designated as *iRadon*, is derived using the polar coordinates of the object in the Fourier domain, a natural choice when varying θ while keeping a fixed structuring frequency f_s. This is illustrated in Fig. 3 for $f_s = 1$ mm^{-1} and $-\frac{\pi}{2} \le \theta \le \frac{\pi}{2}$. This method constitutes a generalization of FBP expressed in Eq. (7). The second method, designated as *iFourier*, is derived using Cartesian coordinates in the Fourier domain. It is well adapted to the ideal case where US waves are structured for multiple discrete values of f_s while θ is fixed. Both methods are fully described hereafter.

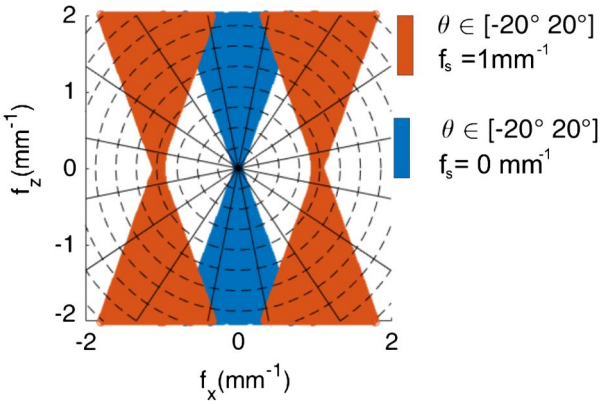

Fig. 2. Exploration of the Fourier plane for the angle-limited case where $-20^\circ \le \theta \le 20^\circ$ and $f_s = 0$ mm^{-1} (blue) and $f_s = 1$ mm^{-1} (orange).

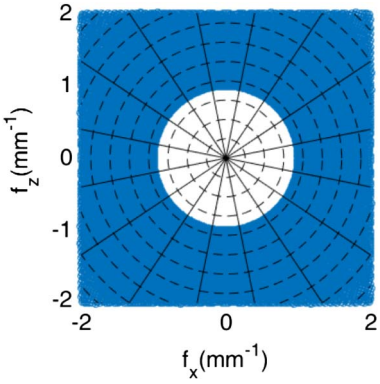

Fig. 3. Exploration of the Fourier plane for the ideal case where $\theta \in [-\pi/2, \pi/2]$ and $f_s = 1$ mm^{-1}.

3. ANALYTIC INVERSION ALGORITHMS

A. iRadon Inversion Method

We adapt the demonstration of the FBP [17] by now supposing that f_s is fixed, while θ can take any value between 0 and 2π in order to generalize Eq. (6). The first step is to switch from a polar to a Cartesian coordinate system. To do so, we calculate the Jacobian matrix J associated with the change of variable defined by F_{f_s}:

$$\mathbf{F}_{f_s}: (f_t, \theta) \in \mathbb{R} \times [0, 2\pi] \rightarrow \begin{cases} f_x(f_t, \theta) = f_t \sin\theta + f_s \cos\theta \\ f_z(f_t, \theta) = f_t \cos\theta - f_s \sin\theta \end{cases}. \quad (11)$$

We find that $\det(J) = -f_t$, which, bearing in mind Eq. (10), allows us to write

$$\int_{\theta=0}^{2\pi}\int_{f_t>0}\tilde{s}(f_t,\theta,f_s)e^{2i\pi(xf_x+zf_z)}f_t\mathrm{d}f_t\mathrm{d}\theta = \int_{\Omega}\mathcal{F}_{x,z}(I)(f_x,f_z)e^{2i\pi(xf_x+zf_z)}\mathrm{d}f_x\mathrm{d}f_z, \quad (12)$$

where Ω is the image of $\mathbb{R}^+ \times [0, 2\pi]$ by function $\mathbf{F}_{f_s}$. As illustrated in Fig. 3, Ω is equal to the Fourier plane deprived from a disk of radius f_s. To fully reconstruct the object, the contribution over the disk is added as expressed in Eq. (13):

$$I(x,z) = \int_{\Omega}\mathcal{F}_{x,z}(I)(f_x,f_z)e^{2i\pi(xf_x+zf_z)}\mathrm{d}f_x\mathrm{d}f_z + \int_{\mathbb{R}^2\setminus\Omega}\mathcal{F}_{x,z}(I)(f_x,f_z)e^{2i\pi(xf_x+zf_z)}\mathrm{d}f_x\mathrm{d}f_z. \quad (13)$$

The second term of this equation can be recovered using the unstructured signal $\tilde{s}(f_t,\theta,0)$, leading to a full expression of the original object:

$$I(x,z) = \int_0^{2\pi}\int_0^{\infty}\tilde{s}(f_t,\theta,f_s)e^{2i\pi z' f_t}e^{2i\pi x' f_s}f_t\mathrm{d}f_t\mathrm{d}\theta + \int_0^{2\pi}\int_0^{f_s}\tilde{s}(f_t,\theta,0)e^{2i\pi z' f_t}f_t\mathrm{d}f_t\mathrm{d}\theta. \quad (14)$$

The integral is then split into two terms $\int_{\theta=0}^{\pi}$ and $\int_{\theta=\pi}^{2\pi}$ followed by a change of variable $\theta \leftarrow \theta - \pi$ on the second term. Making use of the relation $\tilde{s}(f_t,\theta+\pi,f_s) = \tilde{s}(f_t,\theta,f_s)^*$, and limiting the integration domain to $[-\theta_m,\theta_m]$ as it is performed in FBP, Eq. (14) leads to the generalized FBP expression:

$$I_{\mathrm{rec}}(x,z) = \int_{-\theta_m}^{\theta_m}2\Re\left[\int_{\mathbb{R}^+}\tilde{s}(f_t,\theta,f_s)e^{2i\pi z' f_t}e^{2i\pi x' f_s}\right]f_t\mathrm{d}f_t\mathrm{d}\theta + \int_{-\theta_m}^{\theta_m}\int_{-f_s}^{f_s}\tilde{s}(f_t,\theta,0)e^{2i\pi z' f_t}f_t\mathrm{d}f_t\mathrm{d}\theta, \quad (15)$$

where $\Re$ designates the real part. When using this expression, both $\tilde{s}(f_t,\theta,0)$ and $\tilde{s}(f_t,\theta,f_c)$ are multiplied by a Ram-Lak filter [similarly to the FPB described in Eq. (7)], with a cutoff frequency $f_c = 1\ \mathrm{mm}^{-1}$.

B. iFourier Inversion Method

We now suppose an acquisition is performed for all $f_s \in \mathbb{R}$ at a fixed θ value, as illustrated in Fig. 4. We start with the integral, which defines the inverse Fourier transform using Eq. (10), and define the rotation operator of angle θ:

$$\mathbf{R}_\theta : (f_s,f_t) \in \mathbb{R}^2 \rightarrow \begin{cases} f_x(f_s,f_t) = f_t\ \sin\theta + f_s\ \cos\theta \\ f_z(f_s,f_t) = f_t\ \cos\theta - f_s\ \sin\theta \end{cases}. \quad (16)$$

$\mathbf{R}_\theta$ is a unitary operator, and therefore the determinant of its Jacobian matrix is equal to one. This allows a simple change of integration variables in the following expression:

$$\mathcal{F}^{-1}_{f_s,f_t}[s(f_t,\theta,f_s)] = \int_{\mathbb{R}^2}\tilde{s}(f_t,\theta,f_s)e^{2i\pi(xf_s+zf_t)}\mathrm{d}f_s\mathrm{d}f_t = \int_{\mathbb{R}^2}\mathcal{F}_{x,z}(I)(f_x,f_z)e^{2i\pi(x'f_x+z'f_z)}\mathrm{d}f_x\mathrm{d}f_z = I(x',z'). \quad (17)$$

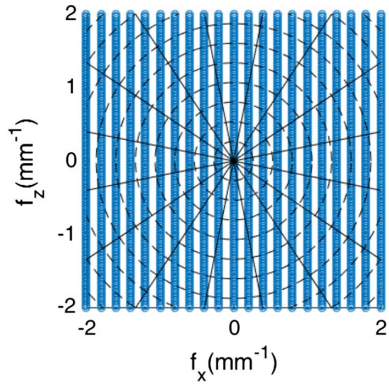

Fig. 4. Exploration of the Fourier plane in the ideal case where $\theta = 0$, $f_s = 0.2n_s\ \mathrm{mm}^{-1}$, with n_s an integer between 0 and 10.

In other words, a full reconstruction of the object at an arbitrary θ value is easily performed by (i) taking the inverse Fourier transform of the signal $s(f_t,\theta,k_s)$, and (ii) rotating the reconstructed object by an angle θ to match the original coordinate system. Because the result is independent of θ, the retroprojection formula is the sum of all reconstructed images, divided by the number N_θ of discrete values in the angular window $[-\theta_m,\theta_m]$. The inversion formula therefore writes

$$I_{\mathrm{rec}}(x,z) = \frac{1}{N_\theta}\sum_{-\theta_m}^{\theta_m}\left[\int_{\mathbb{R}^2}\tilde{s}(f_t,\theta,f_s)e^{2i\pi(x'f_s+z'f_t)}\mathrm{d}f_t\mathrm{d}f_s\right]. \quad (18)$$

To test the validity if both *iRadon* and *iFourier* methods, we wish to calculate Eqs. (15) and (18) when the inversion problem is well-posed. This means either calculate $s(c_s t,\theta,f_s)$ for all angle θ when using *iRadon*, or for all structuring frequencies f_s in the test object support bandwidth when using *iFourier*. We simulate an acquisition on a test object $I(x,z)$ represented in Fig. 5(a). It corresponds to the product of a two-dimensional Gaussian beam with a 0.5 mm wide cross with a $\alpha = 30°$ inner angle, and left-shifted from the center by 2 mm to break the symmetry of the object.

The *iRadon* reconstruction method is tested by evaluating $s(c_s t,\theta,f_s)$ over a full angular span $\theta \in [-\pi/2,\pi/2]$ in the trivial case where $f_s = 0$ (which corresponds to standard FBP) and in the case where $f_s = n_s df_s\ \mathrm{mm}^{-1}$ with $n_s = 10$ and $df_s = 0.24\ \mathrm{cm}^{-1}$. In both cases, the cross is reconstructed and respectively shown in Figs. 5(b) and 5(c).

The same approach is used to validate the *iFourier* inversion, where $s(c_s t,\theta,f_s)$ is evaluated for $f_s = n_s df_s$ where n_s varies in steps of one in the [0, 80] interval. The cross is reconstructed for $\theta = 0°$ in Fig. 5(d) and $\theta = 20°$ in Fig. 5(e), thereby validating the *iFourier* method. Without further proof, we propose hereafter to test both methods on actual experimental data, and compare our results with simulations.

4. EXPERIMENT

A. Experimental Setup

Our experiment was conducted using an Agar gel matrix with dimensions HxLxW $= 5 \times 5 \times 2\ \mathrm{cm}^3$ with 10% concentration

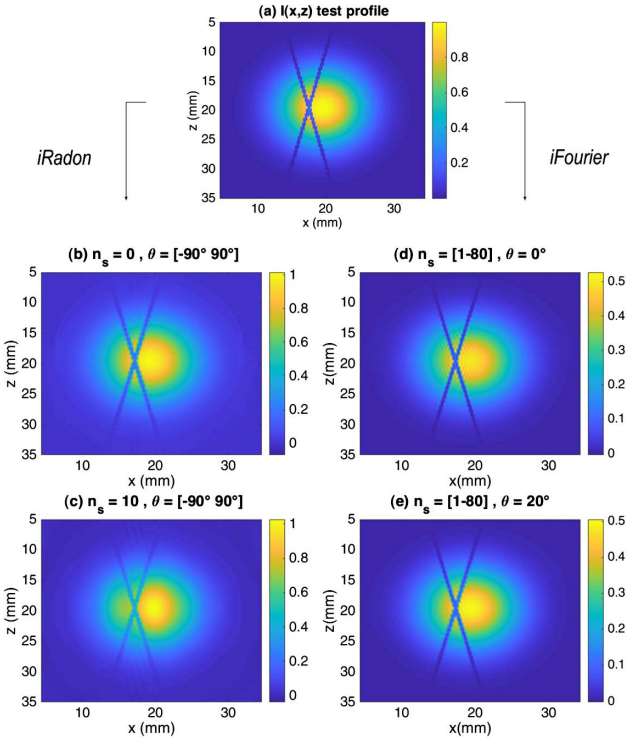

Fig. 5. (a) Original test image where the test object is a 30° angled absorbing cross superimposed on a Gaussian light profile. (b),(c) Reconstruction using *iRadon* method expressed by Eq. (15) for (b) $n_s = 0$ and (c) $n_s = 10$ with $f_s = n_s df_s$ and $df_s = 0.24\ \text{cm}^{-1}$ over full angular span. (d),(e) Reconstruction using *iFourier* method expressed by Eq. (18) where $n_s \in [1, 80]$ when (d) $\theta = 0°$ and (e) $\theta = 20°$.

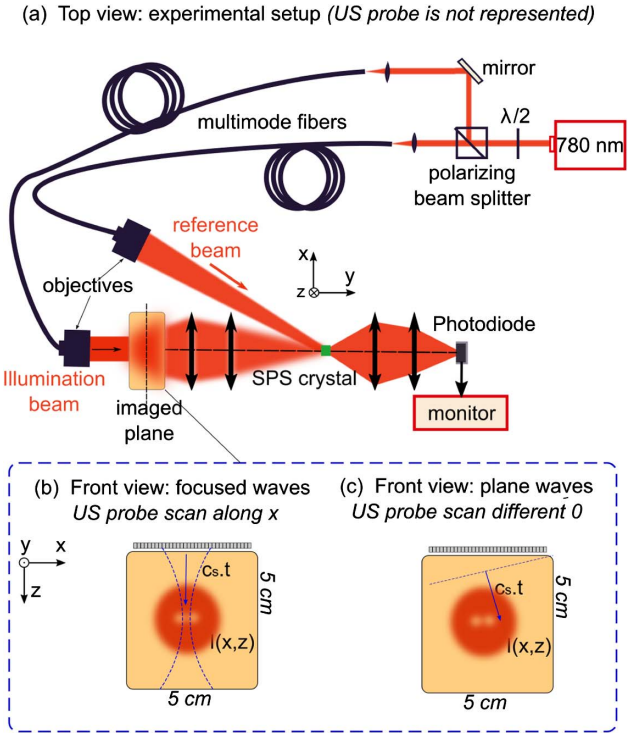

Fig. 6. Experimental setup. (a) Photorefractive detection based on two-wave mixing (reference pulse and transmitted speckle) inside SPS crystal. Signal is collected in transmission of the crystal and focused onto a photodiode for processing. (b) Principle of focused waves, (c) principle of plane waves.

of intralipid. The gel reduced scattering coefficient $\mu_s' \sim 10\ \text{cm}^{-1}$ is similar to that of biological tissues [32]. The method used to make this phantom is described in [9]. Two absorbing inclusions of respectively 2 mm and 3 mm inner diameters were embedded in the middle of the scattering phantom gel and separated by a distance $a \approx 4$ mm. Our light source is a single longitudinal mode tapered-diode centered at 780 nm injected into an amplifier (MOPA, *Sacher Lasertechnik GmBH*). The laser is then divided into two arms with a polarizing beam splitter. On the first arm, the sample is illuminated with 350 mW for a beam diameter ~7 mm, while the other arm is used as a reference beam in our holographic setup, as illustrated in Fig. 6. The acoustic wave used to tag photons is generated with a two-dimensional commercial probe (SL10-2, *Supersonic Imagine, Aix en Provence, France*) driven by a programmable ultrafast US scanner (Aixplorer, *Supersonic Imagine*), where each piezo-element can be arbitrarily addressed. This allows to easily choose among focused, plane, or structured waves by changing the number of active elements along with their relative phase delay. Whichever the selected US spatial structure, the US temporal profile is always one and a half cycle centered at 6 MHz, which corresponds to ~400 μm resolution in the direction of US propagation. Tagged photons are detected in transmission through the gel as depicted in Fig. 6(a) and filtered with a photorefractive holographic setup described in [33]. The AC signal recorded with a Si-photodiode (Thorlabs Det36A - 10MHz bandwidth) is sampled at 10 MHz with an acquisition card (*Gage Digitizer*).

In our experiment, we wish to compare images obtained using FW, PW, and SW. The FW will be considered as our reference. We then demonstrate the increase of spatial resolution when switching from PW to SW. In a SW sequence, θ is varied between -20° and 20°, in steps of 1°, and for each θ value four phases are acquired (cf. Section 2.A) for different integer values n_s, such that $f_s = n_s df_s$, where n_s is an integer and $df_s = 0.24\ \text{cm}^{-1}$ is the sampling frequency. A full sequence is loaded to the US probe operating at 2 kHz, and each sequence is repeated several times to increase the signal-to-noise ratio (SNR) through averaging.

B. Simulation of the Experiment

To test the validity of our reconstruction method, we simulated the propagation of US pulses using FIELDII open source software [34]. Using the geometrical characteristics of our US transducer array, we use FIELDII to calculate the pressure field profile in the imaging plane (x, z). The software relies on a far-field calculation method fully described in [35]. The scattered laser light in that plane is modeled with a Gaussian profile of waist $w_0 = 9$ mm centered at $z = 19.5$ mm, where z is the direction of US propagation defined in Figs. 6(b) and 6(c), and $z = 0$ is set by the US probe transducers position. The position of the Gaussian in our simulation was chosen to match the observed experimental data in the FW configuration.

To model absorbing inclusions, we subtract to this former profile two 80%-deep Gaussian holes with 1 and 1.5 mm respective waists and separated by $a = 4$ mm. MATLAB routines were developed to reproduce the AO experiment by recording the tagged photon signal $s(c_s t, \theta, n_s)$ using the relation defined in Eq. (1). One of the motivations behind simulating our experiment is to generate noise-free data to test both our *iRadon* and *iFourier* inversion algorithms.

5. EXPERIMENTAL RESULTS AND COMPARISON TO SIMULATIONS

A. Lack of Resolution in PW Reconstruction

We first image the absorbing inclusions using FW. The electronic focus was set to $z = 20$ mm, and lines are acquired by scanning direction x in 0.2 mm steps. Each line is averaged 1000 times. This corresponds to an overall acquisition time of 76 s. The result is shown in Fig. 7(a). We observe an excellent qualitative agreement with the simulated image shown Fig. 7(b). A line profile plotted along the black-dotted line is shown in Fig. 7(c) where both inclusions are properly resolved. We measure $a = 4.1 \pm 0.2$ mm in the simulation and $a = 3.8 \pm 0.6$ mm in the experiment. Leaving the position of the test phantom unchanged, we then perform a PW measurement for $-20° \leq \theta \leq 20°$ where each line is also averaged 1000 times, corresponding to an acquisition time of 21 s. Although here PW acquisition is about 4 times faster than FW, the image resulting for standard FBP reconstruction [described by Eq. (7)] suffers from a strong degradation of its lateral resolution, as visible in Fig. 7(d). This behavior is reproduced on simulated data, as shown in Fig. 7(e). This is particularly visible on the line profile plotted in Fig. 7(f) where absorbing inclusions are no longer resolved.

B. Experimental and Simulated Results Using SW

Here, we perform an experiment and simulations with SW for the same angular span as with PW (i.e., $-20° \leq \theta \leq 20°$, with 1° steps) with structuring frequencies $f_s = n_s df_s$, where n_s is an integer varied between 1 and 12 and $df_s = 0.24$ cm^{-1} is the sampling frequency. In order to resolve the two inclusions separated by distance a, structuring frequencies should be around $1/a \sim 0.25$ mm^{-1}, which corresponds to $n_s \sim 10$. Because four frames are acquired at each angle and each n_s according to Eq. (9), we reduce the averaging number to 50 (as opposed to 1000 in the previous experiment), resulting in an overall acquisition time of 51 s. Most of the object spatial information is contained in the acquired raw data. For $n_s > 12$, uncontrolled diffraction effects start to appear on the acoustic wavefront, which leads to degradation of the image (not shown here). This ultimately limits the maximum resolution of this approach to ~3 mm in the present case, as opposed to 1 mm for FW. Here, the SW measurement is performed using enough n_s values to reconstruct the object. The *iFourier* imposes as the natural method to use since the problem is well-posed in that case.

The experimental image reconstructed using the *iFourier* method is shown in Fig. 8(a) and compared to the simulation in Fig. 8(b). Inclusions appear clearly in both images. By plotting in Fig. 8(c) the profile along the black-dotted lines, we measure a separation distance of $a = 4.3 \pm 0.6$ mm in the experiment and $a = 4 \pm 0.2$ mm in the simulation. This distance is, within the error bar, equal to the value previously measured with FW.

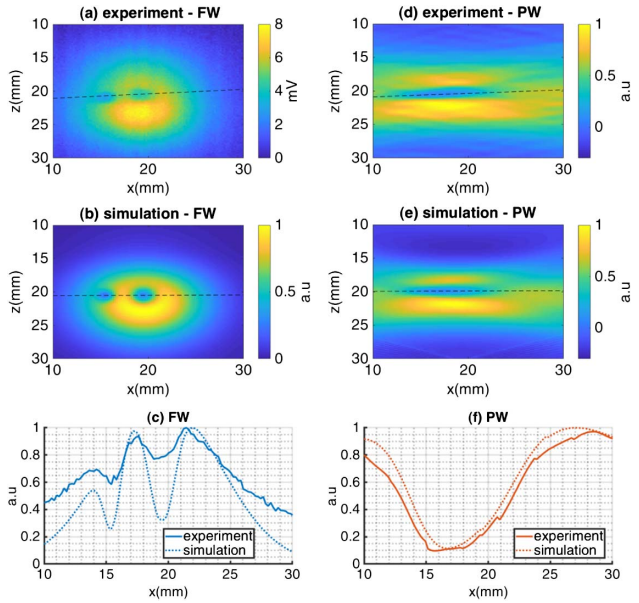

Fig. 7. (a),(b): Respectively experimental and simulated AO image of two embedded absorbers with focused waves (FW). Line profiles along the back dotted line are plotted in (c) in a normalized scale. (d),(e) Respectively experimental and simulated PW reconstructed images for $-20° \leq \theta \leq 20°$ using standard FBP inversion method. Line profiles along the back dotted line are plotted in (f) in normalized scale.

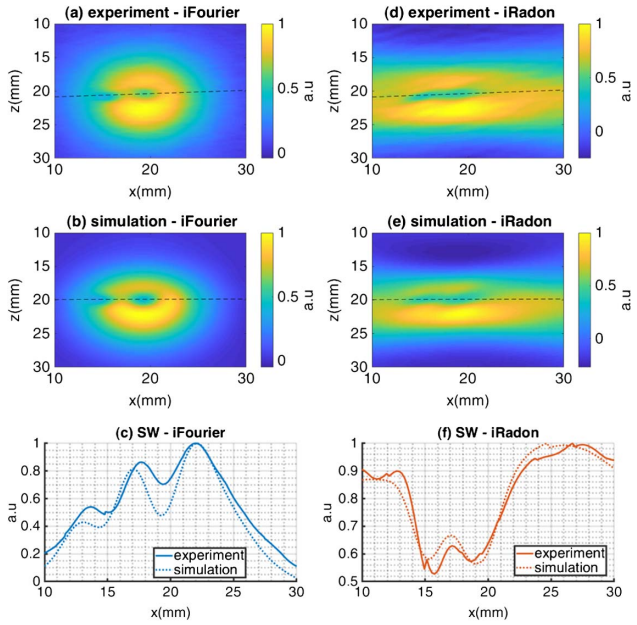

Fig. 8. (a),(b),(d),(e) Respectively experimental and simulated AO image of two embedded absorbers with structured waves (SW) where $n_s \in [1, 12]$ and $-20° \leq \theta \leq 20°$ using (a),(b) *iFourier* or (d),(e) *iRadon* reconstruction methods (on the same acquired raw data). (c),(f) Line profiles along black dotted line for (c) *iFourier* and (f) *iRadon* methods.

On the other hand, when the reconstruction is done using *iRadon*, we observe an elongation of the image in the lateral dimension, as shown in Fig. 8(d). This deformation is reproduced in the simulation shown in Fig. 8(e). Indeed, because the reconstruction problem is now ill-posed, whichever the number of frequencies f_s used, we expect the reconstruction fidelity of *iRadon* to be lesser than *iFourier*. If we plot their respective profiles along the black-dotted lines, it is nevertheless possible to identify two inclusions, as shown in Fig. 8(f) which, as shown in the previous paragraph, cannot be resolved using PW-UOT. We measure $a = 3.2 \pm 0.2$ mm in the experiment and $a = 3.9 \pm 0.6$ mm in the simulation. This result validates our generalized *iRadon* approach exposed in Section 3.A and proves that structuring the US field allows restoration of the lateral resolution of the reconstructed image in spite of the ill-posed nature of the problem.

In a particular application of SW-UOT, one would like to acquire an image with improved lateral resolution while minimizing the number of necessary n_s values. Here, we repeat a SW-UOT acquisition sequence with the same angular span as in the previous paragraph (i.e., $-20° \leq \theta \leq 20°$, with 1° steps) while using only one structuring frequency $f_s = n_s d f_s$, where n_s is fixed to a unique value. We test the reconstruction for $n_s = 8; 9; 10$, and 12 and compare each profile after the reconstruction with that obtained in FW configuration. Each acquisition line is averaged 1000 times, such that the acquisition time is 104 s, namely 5 times the PW acquisition time, or 1.4 the FW acquisition time mentioned in Section 5.A, where the same number of averaging was used. In previous works [11], it was shown that the increase in SNR when switching from FW to PW allows us to decrease the number of required averaging by an order of magnitude. This indicates that SW can still operate at a faster acquisition rate than FW when only one n_s value is used for imaging. Quantitative analyses with respect to SNR and acquisition time regarding SW shall be discussed in future work.

Because only one n_s value is now used to make an image, both *iRadon* and *iFourier* methods address an ill-posed problem. Given the geometry, *iRadon* nonetheless appears to be the natural choice for the reconstruction. Experimental results are shown in Fig. 9, where we plot the reconstructed intensity profile along the inclusions for the different choice of n_s. The profile obtained using FW is plotted as a reference in plain-blue. The first striking result is that both inclusions can be resolved when $n_s = 8$, 9, and 10, and we respectively measure $a = 3.8 \pm 0.2$ mm, $a = 3.2 \pm 0.4$ mm, and $a = 3 \pm 0.4$ mm. When $n_s = 12$, inclusions are no longer visible. This is expected since the US structuring frequency contains very few of the object spectral content. The second striking observation is the existence of small modulations all along the plotted SW profiles. In fact, by choosing only one structuring frequency to perform an image, we prevent out of phase frequency components to interfere destructively along the object profile.

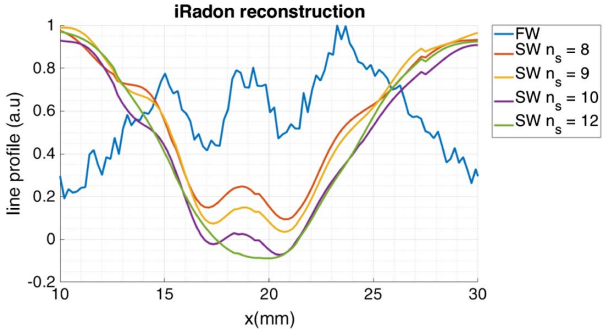

Fig. 9. Experimental 1D profile of the image across the inclusions where we compare focused waves (FW) and structured waves (SW) for unique values of $n_s = 8$; 9; 10 and $n_s = 12$ using the *iRadon* reconstruction method.

6. CONCLUSION

In conclusion, we have demonstrated the possibility to improve the lateral resolution of PW-UOT by adding structure to the spatial envelope of the plane wave used to tag photons. The new formalism behind SW-UOT, which takes into account the US envelope structure, was derived to properly address the problem of image reconstruction. In this respect, we generalized the Fourier slice theorem (only valid for PW) and derived an analytical expression to reconstruct the image. This method was referred to as *iRadon* and corresponds to a generalization of the filtered backprojection method.

Because the angle-limited problem is in general ill-posed, the result of reconstruction is not expected to match the initial object (FW reference image in our case). To test SW-UOT when the problem is well-posed, i.e., when structuring frequencies are covering enough of the object bandwidth, we introduced an alternative inversion method designated as *iFourier*. This method is based on the traditional inverse Fourier transform of the image and appropriate rotation of the image. The successful reconstruct of the object using this method validated the principle of PW-UOT.

Our last experiment and simulations showed it was then possible to resolve two absorbing inclusions separated by 4 mm embedded in a scattering phantom gel using only one structuring frequency of the object bandwidth. Those inclusions could not be resolved with PW-UOT, or for a structuring frequency out of the object bandwidth. One artifact to the reconstruction was, however, a modulation of the image intensity at the structuring frequency along its lateral dimension. This naturally raises the question of improving the reconstruction strategy, for example, by switching from an analytic to an algebraic reconstruction approach. This question remains open and left for future work.

Funding. Institut national de la santé et de la recherche médicale (Inserm) (MALT-C16027HS); Conseil National de la Recherche Scientifique (CNRS) (Défi Instrumentation aux Limites); École Supérieure de Physique et de Chimie Industrielles de la Ville de Paris (ESPCI) (ANR-10-IDEX-0001-02-PSL, ANR-10-LABX-24).

REFERENCES

1. M. S. Patterson, B. Chance, and B. C. Wilson, "Time resolved reflectance and transmittance for the noninvasive measurement of tissue optical properties," Appl. Opt. **28**, 2331–2336 (1989).

2. F. A. Marks, H. W. Tomlinson, and G. W. Brooksby, "A comprehensive approach to breast cancer detection using light: photon localization by ultrasound modulation and tissue characterization by spectral discrimination," Proc. SPIE **1888**, 500–510 (1993).
3. L. Wang, S. L. Jacques, and X. Zhao, "Continuous-wave ultrasonic modulation of scattered laser light to image objects in turbid media," Opt. Lett. **20**, 629–631 (1995).
4. L. V. Wang, "Mechanisms of ultrasonic modulation of multiply scattered coherent light: an analytic model," Phys. Rev. Lett. **87**, 043903 (2001).
5. S. Sakadžić and L. V. Wang, "High-resolution ultrasound-modulated optical tomography in biological tissues," Opt. Lett. **29**, 2770–2772 (2004).
6. Y. Li, H. Zhang, C. Kim, K. H. Wagner, P. Hemmer, and L. V. Wang, "Pulsed ultrasound-modulated optical tomography using spectral-hole burning as a narrowband spectral filter," Appl. Phys. Lett. **93**, 011111 (2008).
7. T. W. Murray, L. Sui, G. Maguluri, R. A. Roy, A. Nieva, F. Blonigen, and C. A. DiMarzio, "Detection of ultrasound-modulated photons in diffuse media using the photorefractive effect," Opt. Lett. **29**, 2509–2511 (2004).
8. F. Ramaz, B. Forget, M. Atlan, A.-C. Boccara, M. Gross, P. Delaye, and G. Roosen, "Photorefractive detection of tagged photons in ultrasound modulated optical tomography of thick biological tissues," Opt. Express **12**, 5469–5474 (2004).
9. J.-B. Laudereau, E. Benoit à La Guillaume, V. Servois, P. Mariani, A. A. Grabar, M. Tanter, J.-L. Gennisson, and F. Ramaz, "Multi-modal acousto-optic/ultrasound imaging of *ex vivo* liver tumors at 790 nm using a $Sn_2P_2S_6$ wavefront adaptive holographic setup," J. Biophotonics **8**, 429–436 (2015).
10. M. Bocoum, J. L. Gennisson, C. Venet, M. Chi, P. M. Petersen, A. A. Grabar, and F. Ramaz, "Two-color interpolation of the absorption response for quantitative acousto-optic imaging," Opt. Lett. **43**, 399–402 (2018).
11. J.-B. Laudereau, A. A. Grabar, M. Tanter, J.-L. Gennisson, and F. Ramaz, "Ultrafast acousto-optic imaging with ultrasonic plane waves," Opt. Express **24**, 3774–3789 (2016).
12. J. Baruchel, J.-Y. Buffiere, and E. Maire, *X-ray Tomography in Material Science* (Hermes Science Publications, 2000).
13. D. L. Bailey, M. N. Maisey, D. W. Townsend, and P. E. Valk, *Positron Emission Tomography* (Springer, 2005).
14. J. Frank, *Electron Tomography: Methods for Three-Dimensional Visualization of Structures in the Cell* (Springer Science & Business Media, 2008).
15. P. Subbarao, P. Munshi, and K. Muralidhar, "Performance of iterative tomographic algorithms applied to non-destructive evaluation with limited data," NDT & E Int. **30**, 359–370 (1997).
16. A. K. Hara, R. G. Paden, A. C. Silva, J. L. Kujak, H. J. Lawder, and W. Pavlicek, "Iterative reconstruction technique for reducing body radiation dose at CT: feasibility study," Am. J. Roentgenol. **193**, 764–771 (2009).
17. A. C. Kak and M. Slaney, *Principles of Computerized Tomographic Imaging* (IEEE, 1988).
18. A. H. Delaney and Y. Bresler, "Globally convergent edge-preserving regularized reconstruction: an application to limited-angle tomography," IEEE Trans. Image Process. **7**, 204–221 (1998).
19. R. Rangayyan, A. P. Dhawan, and R. Gordon, "Algorithms for limited-view computed tomography: an annotated bibliography and a challenge," Appl. Opt. **24**, 4000–4012 (1985).
20. J. Frikel, "Sparse regularization in limited angle tomography," Appl. Comput. Harmon. Anal. **34**, 117–141 (2013).
21. R. Heintzmann and C. G. Cremer, "Laterally modulated excitation microscopy: improvement of resolution by using a diffraction grating," Proc. SPIE **3568**, 185–197 (1999).
22. M. G. Gustafsson, "Surpassing the lateral resolution limit by a factor of two using structured illumination microscopy," J. Microsc. **198**, 82–87 (2000).
23. R. Heintzmann and T. Huser, "Super-resolution structured illumination microscopy," Chem. Rev. **117**, 13890–13908 (2017).
24. M. Lesaffre, S. Farahi, M. Gross, P. Delaye, A. Boccara, and F. Ramaz, "Acousto-optical coherence tomography using random phase jumps on ultrasound and light," Opt. Express **17**, 18211–18218 (2009).
25. K. Barjean, K. Contreras, J.-B. Laudereau, É. Tinet, D. Ettori, F. Ramaz, and J.-M. Tualle, "Fourier transform acousto-optic imaging with a custom-designed CMOS smart-pixels array," Opt. Lett. **40**, 705–708 (2015).
26. K. Barjean, F. Ramaz, and J.-M. Tualle, "Theoretical study of Fourier-transform acousto-optic imaging," J. Opt. Soc. Am. A **33**, 854–862 (2016).
27. M. Kempe, M. Larionov, D. Zaslavsky, and A. Genack, "Acousto-optic tomography with multiply scattered light," J. Opt. Soc. Am. A **14**, 1151–1158 (1997).
28. F. Natterer and F. Wübbeling, *Mathematical Methods in Image Reconstruction* (SIAM, 2001), Vol. **5**.
29. S. Lévêque-Fort, "Three-dimensional acousto-optic imaging in biological tissues with parallel signal processing," Appl. Opt. **40**, 1029–1036 (2001).
30. M. Gross and M. Atlan, "Digital holography with ultimate sensitivity," Opt. Lett. **32**, 909–911 (2007).
31. S. Lai, B. King, and M. A. Neifeld, "Wave front reconstruction by means of phase-shifting digital in-line holography," Opt. Commun. **173**, 155–160 (2000).
32. J. Mobley and T. Vo-Dinh, "Optical properties of tissue," in *Biomedical Photonics Handbook* (CRC Press, 2003), Vol. **2**, pp. 1–2.
33. S. Farahi, G. Montemezzani, A. A. Grabar, J.-P. Huignard, and F. Ramaz, "Photorefractive acousto-optic imaging in thick scattering media at 790 nm with a $Sn_2P_2S_6$:Te crystal," Opt. Lett. **35**, 1798–1800 (2010).
34. J. A. Jensen, "A model for the propagation and scattering of ultrasound in tissue," J. Acoust. Soc. Am. **89**, 182–190 (1991).
35. J. A. Jensen and N. B. Svendsen, "Calculation of pressure fields from arbitrarily shaped, apodized, and excited ultrasound transducers," IEEE Trans. Ultrason., Ferroelectr., Freq. Control **39**, 262–267 (1992).